electronics

MDPI

Article

Bandwidth-Invariant MTPA Speed Control of Induction Motor Drives with Application to Airborne Wind Energy Systems

Carolina Nicolás-Martín *, David Santos-Martín, Jorge González-García and Miguel Alonso-Resta

Department of Electrical Engineering, Universidad Carlos III de Madrid, 28911 Leganés, Spain; dsmartin@ing.uc3m.es (D.S.-M.); jorgegga@ing.uc3m.es (J.G.-G.); miguel.a.resta@alumnos.uc3m.es (M.A.-R.)
* Correspondence: canicola@ing.uc3m.es

Abstract

Efficiency-oriented control of induction motor drives reduces rotor flux at partial load, but the resulting reduction in speed-loop gain degrades closed-loop bandwidth under fixed-gain control. The maximum torque per ampere (MTPA) constraint allows an exact resolution of this trade-off. Enforcing MTPA as a structural control law reduces the conventional two-input field-oriented-control plant to a single-input single-output system. Its linearized transfer function is a second-order plant with a real zero at twice the rotor-flux pole frequency. A gain-scheduled proportional–integral controller, whose gain is inversely proportional to the MTPA operating-point current, cancels the operating-point dependence and maintains constant crossover frequency and phase margin without an additional flux observer or look-up table. Four strategies are compared in simulation and experimentally on an 18.5 kW induction machine under airborne-wind-energy pumping cycles: standard field-oriented control, fixed-gain MIMO-MTPA, the proposed SISO-MTPA, and loss minimization. SISO-MTPA is the only strategy that improves both net harvested energy and speed tracking relative to the FOC baseline while remaining undominated: its energy is within 10% of the MTPA-optimal strategies, its speed-error RMSE is approximately 1.7 times lower, and its maximum deviation is over 40% lower. Against an industrial drive under high-power generation, it reduces speed-tracking RMSE by 47% with comparable generated energy.

Keywords: maximum torque per ampere; induction motor; field-oriented control; bandwidth invariance; gain scheduling; loss minimization; airborne wind energy; pumping cycle

1. Introduction

Field-oriented control (FOC) of induction motors (IMs) is the established standard for high-performance variable-speed drives in industrial and traction applications [1,2]. In its conventional rotor-flux-oriented form, the controller maintains the rotor flux magnitude at its rated value while independently regulating the torque-producing current component. This decoupled structure gives a nearly constant-gain speed plant and excellent dynamic response. Its efficiency drawback is equally familiar: rated flux is retained even when the requested torque is small, so magnetizing current and iron loss remain unnecessarily high during partial-load operation. This limitation has motivated both model-based loss minimization and simpler search or mapping strategies [3–12].

Among the various optimization approaches, the maximum torque per ampere (MTPA) strategy minimizes the stator current magnitude for a given electromagnetic torque, reducing stator copper losses to their theoretical minimum. The foundational MTPA formulation

Check for updates

Academic Editors: Chengbo Yang, Yuanlong Xie and Mingjin Hu

Received: 17 September 2026
Revised: 14 October 2026
Accepted: 16 October 2026
Published: 22 October 2026

Copyright: © 2026 by the authors. Licensee MDPI, Basel, Switzerland. This article is an open access article distributed under the terms and conditions of the Creative Commons Attribution (CC BY) license.

for induction motors was established by [13], who proposed a slip-speed-based control strategy within an indirect FOC framework. Under the assumption of a linear magnetic circuit in the rotor-flux-oriented reference frame, the steady-state MTPA condition for squirrel-cage IMs yields the remarkably simple relationship $i_{sd} = |i_{sq}|$, meaning the flux-producing and torque-producing current components must be equal in magnitude. This condition is notably independent of machine parameters (a consequence of the symmetric magnetizing inductance in both axes) and represents a 45° current angle in the dq plane [14].

While the steady-state benefits of MTPA are well established, the dynamic implications of coupling the flux and torque channels through a single variable have received less rigorous analytical treatment. The core challenge lies in the rotor time constant $\tau_r = L_{rr}/R_r$, which governs the rate at which rotor flux can be built up or reduced. In conventional FOC, this slow dynamics is confined to the flux channel and does not affect the torque response, since the flux is held constant. Under MTPA operation, however, every change in torque demand simultaneously requires a change in flux level, introducing a remagnetization transient that fundamentally limits the achievable speed control bandwidth.

Several advanced strategies address MTPA dynamics in IM drives. Feedback-linearization approaches [15–18] establish asymptotic torque tracking at the MTPA point and can compensate selected nonlinear effects, but the rotor-flux transient still limits how rapidly the operating point can move. Constraint-aware extensions incorporate voltage limits [19], while iron-loss models support maximum-torque-per-watt operation [20]. Fractional-order PI control [21] and model predictive control [14,22] can substantially reduce stator current, although their reported speed response reflects the same underlying flux–torque coupling. These methods are valuable when nonlinear constraints or multivariable objectives dominate, but their tuning and implementation do not directly expose a simple speed-loop bandwidth rule.

A common thread is that the MTPA control problem is treated as an inherently multivariable nonlinear system, with designs based on Lyapunov arguments, passivity, feedback linearization, or predictive optimization [14,23]. Those frameworks offer rigorous stability or constraint handling, but they do not isolate the small-signal speed plant created specifically by the MTPA equality, nor do they yield a direct algebraic rule that keeps its bandwidth independent of load.

This recurring trade-off is not incidental but structural. The gain of the speed-loop plant is proportional to the rotor flux, $G \propto K\lambda_{rd}/J$, and every efficiency-oriented strategy operates precisely by reducing λ_{rd} at partial load. With fixed controller gains, the loop gain (and hence the crossover frequency) drops in direct proportion to the flux reduction: efficiency optimization degrades the closed-loop bandwidth *by construction*, not by implementation. The central result of this paper is that, under the MTPA constraint specifically, this conflict admits an exact resolution within the adopted small-signal model (ideal inner-current control, linear magnetic circuit, operation below the MTPA torque limit). The constraint $i_{sd} = |i_{sq}|$ collapses the operating-point dependence of the plant gain to a linear function of a single operating-point variable, which a gain-scheduled PI cancels algebraically, restoring bandwidth invariance without sacrificing MTPA efficiency, without an additional flux observer in the speed loop, and without look-up tables.

Airborne wind energy systems (AWES) represent an emerging technology that harvests wind resources at altitudes beyond the reach of conventional turbines [24–27]. In ground-generation systems, a tethered kite or rigid wing pulls a tether off a winch coupled to an electrical generator during the *reel-out* phase; during the *reel-in* phase, the tether is retracted under reduced loading [28–30]. This pumping cycle requires four-quadrant operation with torque reversals every few tens of seconds [31]. Squirrel-cage IMs suit the ground-station drive for their robustness, low cost, and independence from rare-earth

magnets [32]. Because the cycle spends much of its time at partial load, MTPA is particularly attractive [13], yet the periodic torque oscillations and the flux transients it introduces place stringent demands on the dynamic response. Although AWES provides the motivating application of this work, the underlying control challenge (sustained partial-load operation with recurrent load transients) is shared by a broader class of cyclic drives, including hoisting and winching systems, wave-energy converters, and press servo drives, to which the proposed analysis applies directly.

Prior AWES ground-station control studies have used cascaded architectures (e.g., sliding-mode speed control with rotor-flux-oriented current regulation), validated emulation test benches and converter controls, and nonlinear/MPC approaches for kite trajectory and winch-speed loops [29,31,33]. However, AWES literature has not examined how MTPA affects the drive's electromechanical dynamics, nor provided an analytical characterization of the bandwidth limit imposed by the rotor time constant under the MTPA constraint.

The main contributions of this paper are as follows:

1. Load-invariant speed-loop bandwidth under MTPA: A gain-scheduled PI controller is proposed with $K_p = 1/(\Gamma \cdot u_0)$, where Γ is a single analytically derived constant. The scheduling law algebraically cancels the operating-point dependence of the MTPA plant gain, maintaining constant crossover frequency and phase margin across the operating range. This is a structural property, an exact algebraic cancellation, rather than a numerical improvement: among the efficiency-oriented strategies compared, it is the only one whose closed-loop bandwidth is independent of the operating point.
2. SISO plant model under the MTPA constraint: By enforcing the MTPA condition $i_{sd} = |i_{sq}| \triangleq i_s$ as a structural control law, the conventional two-input FOC plant is reduced to a single-input system. The linearized transfer function from i_s to ω_m is analytically derived, yielding a second-order plant with poles at $s = -1/\tau_r$ and $s = -B/J$, and a real zero at $s = -2/\tau_r$. This model explains the dynamic effect of coupling flux and torque production through a single current variable.
3. Efficiency–tracking–complexity comparison: The proposed SISO-MTPA is compared against classical FOC, fixed-gain MIMO-MTPA, and a loss-minimization benchmark on an 18.5 kW IM drive. Simulation and experiments show that SISO-MTPA is the only strategy that improves both energy and tracking over the FOC baseline. It thus offers the best overall trade-off: near-MTPA-optimal energy (within 10%) with approximately 1.7 times lower speed-error RMSE than the higher-energy optimized strategies, from a simple implementation without look-up tables.

The remainder of the paper is organized as follows. Section 2 presents the rotor-flux-oriented IM model and MTPA condition; Section 3 derives and analyzes the SISO plant; Section 4 details the gain-scheduled PI design; Section 5 introduces the competing strategies and the crossover-frequency analysis; Sections 6 and 7 report the simulation and experimental validation and Section 8 concludes.

2. Induction Motor Model and MTPA Condition

2.1. Field-Oriented Control Framework

In the rotor-flux-oriented dq reference frame, assuming ideal current control in the inner loop, an approximation justified by the ~75:1 bandwidth separation between the current loop (~1500 rad/s) and the speed loop (20 rad/s), the relevant dynamic equations for the outer loops are as follows:

$$\dot{\lambda}_{rd} = \frac{L_m}{\tau_r} i_{sd} - \frac{1}{\tau_r} \lambda_{rd} \tag{1}$$

$$T_e = K \lambda_{rd} \cdot i_{sq} \tag{2}$$

$$J \dot{\omega}_m = T_e + T_L - B \omega_m \tag{3}$$

where $K = \frac{3}{2} p \frac{L_m}{L_{rr}}$ is the torque constant and $\tau_r = L_{rr}/R_r$ the rotor time constant (symbols in the Nomenclature; values in Table 1). The load torque T_L denotes the tether torque applied by the cable on the winch drum; since the tether can only pull, $T_L \geq 0$ at all times, and torque oscillations occur entirely on the electrical side through T_e. The electrical and mechanical parameters of the drive are listed in Table 1.

Table 1. Electrical and Mechanical Parameters of the Siemens 1LG4 186-4AA Induction Motor.

Parameter	Symbol	Value	Unit
Rated power	P_n	18.5	kW
Number of pole pairs	p	2	–
Magnetizing inductance	L_m	40.83	mH
Total rotor inductance	L_{rr}	45.11	mH
Rotor resistance	R_r	0.11	Ω
Stator resistance	R_s	0.22	Ω
Total moment of inertia	J	0.27	kg m^2
Viscous-friction coefficient	B	0.013	N m s/rad
Rotor–stator coupling factor	$k = L_m/L_{rr}$	0.9051	–
Rated d-axis stator current	$i_{sd,\mathrm{nom}}$	23	A
Rated rotor flux linkage	$\lambda_{rd}^{\mathrm{nom}}$	0.94	Wb
Rotor time constant	τ_r	410	ms
Mechanical time constant	τ_m	20.8	s
Iron-loss model coefficient	c_{Fe}	0.003	W s^2/Wb^2

2.2. Derivation of the MTPA Condition

At steady state, the flux equation gives $\lambda_{rd} = L_m i_{sd}$, and substitution into the torque equation gives $T_e = K_T i_{sd} i_{sq}$, where $K_T = K L_m$. For a prescribed electromagnetic torque, maximum torque per ampere is, therefore, equivalent to minimizing the squared stator-current magnitude $|\boldsymbol{i}_s|^2 = i_{sd}^2 + i_{sq}^2$. The constrained optimization problem is

$$\min_{i_{sd}, i_{sq}} \left(i_{sd}^2 + i_{sq}^2 \right) \quad \text{s.t.} \quad K_T \, i_{sd} \, i_{sq} = T_e \tag{4}$$

The first-order optimality conditions $2 i_{sd} = \mu K_T i_{sq}$ and $2 i_{sq} = \mu K_T i_{sd}$, where μ is the Lagrange multiplier, yield $i_{sd}^2 = i_{sq}^2$. Positive d-axis current is retained to establish rotor flux, whereas the sign of i_{sq} selects motoring or generating torque. Thus, the MTPA condition is

$$i_{sd} = |i_{sq}| \tag{5}$$

This result is independent of machine parameters under the assumed linear magnetic circuit. Defining the unified nonnegative current $i_s \triangleq i_{sd} = |i_{sq}|$ makes the current magnitude $|\boldsymbol{i}_s| = \sqrt{2} i_s$ and the steady-state torque

$$T_e = K_T i_s^2 \cdot \mathrm{sign}(i_{sq}) \tag{6}$$

so that the minimum stator-current magnitude required for a specified torque is $|\boldsymbol{i}_s|_{\min} = \sqrt{2|T_e|/K_T}$.

2.3. From Two Independent Current Commands to One Input

Enforcing (5) as a structural control law removes one degree of freedom from the conventional multiple-input FOC formulation. The speed controller no longer requests torque current independently of a separate flux reference; it requests the single unified current i_s, and the current-reference generator assigns $i_{sd}^* = i_s^*$ and $i_{sq}^* = i_s^* \operatorname{sign}(T_e^*)$. A change in this command, therefore, acts through two simultaneous paths: it changes torque directly through i_{sq} at the existing rotor flux, and it changes torque indirectly by modifying the rotor flux through i_{sd}. Because the indirect path contains the rotor time constant, the resulting speed plant is not the first-order constant-gain model used for classical FOC. The following section derives its nonlinear state representation and its operating-point linearization.

3. SISO Plant Under MTPA Constraint

3.1. Nonlinear State-Space Model

Substituting $i_{sd} = i_s$ and $i_{sq} = i_s$ into (1)–(3) yields the two-state, single-input system:

$$\dot{x}_1 = -\frac{1}{\tau_r} x_1 + \frac{L_m}{\tau_r} u \tag{7}$$

$$\dot{x}_2 = \frac{K}{J} x_1 u - \frac{B}{J} x_2 + \frac{1}{J} d \tag{8}$$

where $x_1 = \lambda_{rd}$ is the rotor-flux state, $x_2 = \omega_m$ is the mechanical-speed state, $u = i_s$ is the unified current command, and $d = T_L$ is the load-torque disturbance. The product $x_1 u$ in (8) is bilinear: the same input that changes the flux state also multiplies that state in the torque expression. This is the essential nonlinear coupling introduced by enforcing MTPA dynamically.

3.2. Equilibrium and Small-Signal Linearization

For a constant operating current u_0 and constant load torque T_{L0}, the steady-state equilibrium is

$$\lambda_{rd}^0 = L_m u_0, \qquad \omega_m^0 = \frac{K_T u_0^2 \operatorname{sign}(i_{sq}) + T_{L0}}{B} \tag{9}$$

where the superscript 0 denotes an equilibrium value. Writing each variable as its equilibrium value plus a perturbation and discarding products of perturbations gives the following small-signal model; $\Delta(\cdot)$ denotes deviation from the operating point:

$$\begin{bmatrix} \Delta\dot{x}_1 \\ \Delta\dot{x}_2 \end{bmatrix} = \underbrace{\begin{bmatrix} -\frac{1}{\tau_r} & 0 \\ \frac{K u_0}{J} & -\frac{B}{J} \end{bmatrix}}_{\boldsymbol{A}} \begin{bmatrix} \Delta x_1 \\ \Delta x_2 \end{bmatrix} + \underbrace{\begin{bmatrix} \frac{L_m}{\tau_r} \\ \frac{K L_m u_0}{J} \end{bmatrix}}_{\boldsymbol{b}_u} \Delta u \tag{10}$$

The lower-triangular structure of $\boldsymbol{A}$ reveals unidirectional coupling: flux dynamics affect speed, but speed does not affect flux under perfect rotor-flux orientation.

3.3. Transfer Function

Computing $G(s) = \boldsymbol{c}(s\boldsymbol{I} - \boldsymbol{A})^{-1}\boldsymbol{b}_u$ with $\boldsymbol{c} = [0 \;\; 1]$, the determinant of the resolvent is

$$\det(s\boldsymbol{I} - \boldsymbol{A}) = \left(s + \frac{1}{\tau_r}\right)\left(s + \frac{B}{J}\right), \tag{11}$$

whereas the input vector multiplied by the adjugate is

$$\mathrm{adj}(s\boldsymbol{I}-\boldsymbol{A})\boldsymbol{b}_u = \begin{bmatrix} \dfrac{L_m}{\tau_r}\left(s+\dfrac{B}{J}\right) \\ \dfrac{KL_m u_0}{J}\left(s+\dfrac{2}{\tau_r}\right) \end{bmatrix}. \tag{12}$$

The second component contains both the direct torque-current path and the indirect flux-mediated path. Their sum produces the main analytical result:

$$G(s) = \frac{\Delta\omega_m(s)}{\Delta i_s(s)} = \frac{KL_m u_0}{J}\,\frac{s+z_1}{(s+p_1)(s+p_2)} \tag{13}$$

where

$$z_1 = \frac{2}{\tau_r}, \qquad p_1 = \frac{1}{\tau_r}, \qquad p_2 = \frac{B}{J} \tag{14}$$

The zero z_1 is exactly twice the flux pole p_1, a direct consequence of the dual actuation path created by the MTPA constraint. The numerator of (13) is the sum of two contributions to the speed response:

$$\underbrace{\left(s+\frac{1}{\tau_r}\right)\frac{KL_m u_0}{J}}_{\text{direct (via } i_{sq})} + \underbrace{\frac{Ku_0}{J}\cdot\frac{L_m}{\tau_r}}_{\text{flux (via } i_{sd})} = \frac{KL_m u_0}{J}\left(s+\frac{2}{\tau_r}\right) \tag{15}$$

The first contribution is the immediate torque change through i_{sq} at the existing flux level; the second is the delayed torque change produced as i_{sd} modifies the rotor flux. Their superposition changes the numerator from $s + 1/\tau_r$ to $s + 2/\tau_r$.

3.4. Origin and Interpretation of the Plant Zero

The finite zero at $s = -2/\tau_r$ is a stable, real transmission zero created by the coupled actuation described above. It should not be interpreted as a sinusoidal cancellation frequency: its location is on the negative real axis, not at $j2/\tau_r$. In frequency-response terms, the zero begins adding magnitude and phase lead around $2/\tau_r$, while the rotor-flux pole at $1/\tau_r$ contributes lag at a nearby, lower frequency. The combined pole–zero pair, therefore, modifies the mid-frequency disturbance response without introducing nonminimum-phase behavior.

3.5. Pole-Zero Structure and Bandwidth Implications

For typical IMs, the poles and zeros of (13) satisfy $|p_2| \ll |p_1| < |z_1|$, so the zero provides phase lead rather than lag, in contrast to the classical FOC plant $G_{\mathrm{FOC}}(s) = K\lambda_{rd}^{\mathrm{nom}}/(Js+B)$, with $\lambda_{rd}^{\mathrm{nom}}$ the rated rotor flux, which has no finite zeros.

The pole-zero doublet at $1/\tau_r$ and $2/\tau_r$ shapes the mid-frequency response. While the zero provides phase lead, the nearby pole partially cancels this benefit. For the 18.5 kW motor with $\tau_r = 410$ ms, the doublet spans frequencies between 2.4 and 4.9 rad/s, well below the design crossover frequency $\omega_c = 20$ rad/s. At crossover, the doublet contributes only a modest phase deficit (PM = 83° versus 90° for the classical FOC plant), but it provides significant gain enhancement in the 2–5 rad/s disturbance frequency band, which proves advantageous for wind gust rejection (Section 6.6).

Table 2 collects the structural differences. Relative to the first-order, linear time-invariant (LTI) FOC plant, the SISO-MTPA plant is second-order and linear parameter-varying (LPV): its poles and zeros are fixed by machine parameters, but its gain is proportional to u_0. That especially simple form of parameter variation is what makes exact gain scheduling possible.

Table 2. Structural Comparison of the Classical FOC and SISO-MTPA Speed Plants.

Property	Classical FOC	SISO-MTPA
Plant order	First order	Second order
Poles	$-B/J$	$-B/J, -1/\tau_r$
Finite zeros	None	$-2/\tau_r$
DC gain	$K\lambda_{rd}^{\mathrm{nom}}/B$	$2KL_m u_0/B$
Operating-point dependence	Constant gain	Gain linear in u_0
Small-signal model class	LTI	LPV through the gain
Nominal phase margin [a]	90°	83°

[a] At $\omega_c = 20\,\mathrm{rad/s}$ with ideal cancellation of the slow mechanical pole. The implemented integral-time cap gives the values reported in Figure 2.

4. Gain-Scheduled PI Design for the SISO-MTPA Plant

4.1. Controller Structure and Integral Time Constant

A PI controller with anti-windup, $C(s) = K_p(1 + 1/(\tau_i s))$, is employed; the design variables are K_p, τ_i, and the scheduling law $K_p(u_0)$. The PI zero is nominally placed to cancel the slow mechanical pole at $-B/J$ ($\tau_i = J/B = \tau_m$), removing the dominant time constant from the loop and leaving the faster flux dynamics as the bandwidth-limiting factor. For machines with low viscous friction, however, τ_m can exceed tens of seconds, so the integral time is capped as $\tau_i = \min(J/B,\ \tau_i^{\max})$, with $\tau_i^{\max} = 1\,\mathrm{s}$ in the experimental implementation. Since $B/J \approx 0.05\,\mathrm{rad/s} \ll \omega_c$, the inexact cancellation has negligible effect on the crossover frequency and phase margin, while the integral gain is restored by a factor $\tau_m/\tau_i^{\max} \approx 21$, avoiding the sluggish recovery from load-torque steps characteristic of pole-cancellation tuning when B is small. A two-degree-of-freedom structure with a reference-shaping filter would remove the reference-step overshoot; in cyclic drives, however, the dominant excitation is the load disturbance $T_L(t)$ rather than the essentially constant speed reference, and a reference filter does not alter the disturbance response, so the capped-τ_i PI provides the relevant performance with a simpler tuning. With this choice, the open-loop transfer function simplifies to the following:

$$L(s) = C(s)\,G(s) = \frac{K_p K L_m u_0}{J} \cdot \frac{s + 2/\tau_r}{s\,(s + 1/\tau_r)} \tag{16}$$

4.2. Crossover Frequency and Gain Scheduling

Setting $|L(j\omega_c)| = 1$ in (16) and solving for K_p yields the following:

$$K_p = \frac{1}{\Gamma(\omega_c) \cdot u_0} \tag{17}$$

where $\Gamma(\omega_c)$ depends only on machine parameters and the design crossover frequency:

$$\Gamma(\omega_c) = \frac{K L_m}{J\omega_c} \cdot \frac{\sqrt{\omega_c^2 + (2/\tau_r)^2}}{\sqrt{\omega_c^2 + (1/\tau_r)^2}} \tag{18}$$

The key structural property is that the product $K_p \cdot u_0 = 1/\Gamma$ is a constant, independent of the operating point. This exact algebraic cancellation maintains a constant crossover frequency and phase margin regardless of the load, and constitutes the gain-scheduling law proposed in this paper.

4.3. Phase Margin Analysis

With the pole-zero cancellation at $-B/J$, the open loop (16) contains an integrator ($-90°$), the plant zero at $-2/\tau_r$ (phase lead), and the flux pole at $-1/\tau_r$ (phase lag); evaluating $\arg L(j\omega_c)$ yields the phase margin:

$$\mathrm{PM} = 90^\circ + \arctan\left(\frac{\omega_c}{2/\tau_r}\right) - \arctan\left(\frac{\omega_c}{1/\tau_r}\right) \tag{19}$$

For $\omega_c = 20\,\mathrm{rad/s}$, $\mathrm{PM} = 90^\circ + 76.3^\circ - 83.0^\circ = 83.3^\circ$, which provides excellent robustness. The capped integral time of the implementation (Section 4.1) leaves the slow pole at $-B/J$ only approximately canceled, lowering this to $\approx 80^\circ$ in Figure 2, still highly robust. Notably, the phase margin is independent of u_0, confirming the gain-scheduling strategy. This is a frozen-parameter (pointwise) result, standard in gain-scheduled design; its validity for the time-varying loop rests on the scheduling variable changing slowly relative to the closed-loop dynamics. Here the scheduling variable follows the tether-force variations, whose dominant content lies at a few rad/s, well below ω_c, and the experiments of Section 7, with repeated tether-force oscillations, show no loss of stability or tracking performance.

4.4. Flux Floor and Torque Reserve

A minimum current $i_s^{\min}$ is enforced to prevent demagnetization and loss of controllability as $u_0 \to 0$:

$$i_s^{\min} \geq \sqrt{\frac{T_e^{\min}}{K_T}} \tag{20}$$

where $T_e^{\min}$ is the minimum instantaneous torque reserve required for disturbance rejection. This floor corresponds to a minimum flux level $\lambda_{rd}^{\min} = L_m i_s^{\min}$ and prevents the gain-scheduling singularity. In the simulations of Section 6, a torque reserve of $T_e^{\min} = 5\,\mathrm{N\,m}$ is used, yielding $i_s^{\min} \approx 7\,\mathrm{A}$ and $\lambda_{rd}^{\min} = 274\,\mathrm{mWb}$.

In implementation, the equilibrium variable u_0 in (17) is replaced by the scheduling estimate

$$u_{0,\mathrm{sched}} = \max\left(\frac{\hat{\lambda}_{rd}}{L_m}, i_s^{\min}\right),$$

where $\hat{\lambda}_{rd}$ is the rotor-flux estimate already available from the current-model observer used for field orientation. The real-time gain-scheduling law is, therefore,

$$K_p = \frac{1}{\Gamma \cdot u_{0,\mathrm{sched}}}.$$

Because this scheduling variable is derived from the rotor-flux estimate rather than directly from the measured current magnitude, PWM switching ripple in the current measurement does not directly modulate K_p.

4.5. Parameter Sensitivity

The scheduling constant Γ depends on the machine parameters through $K_T = \frac{3}{2} p L_m^2 / L_{rr}$ and $\tau_r = L_{rr}/R_r$, both of which vary in operation: R_r increases with rotor temperature (up to +40%), and L_m decreases with magnetic saturation at high flux (typically -10 to -20%). Two properties make the proposed law robust to these variations. First, above the pole-zero doublet ($\omega_c \gg 2/\tau_r$) the loop magnitude is dominated by $K_p K_T u_0/(J\omega)$, so a mismatch in K_T relocates the crossover proportionally (a -20% saturation-induced error in L_m yields $\omega_c \approx 15.6\,\mathrm{rad/s}$ instead of $20\,\mathrm{rad/s}$) but cannot reintroduce load dependence: the product $K_p \cdot u_0$ remains constant, so the invariance property is structural, not parametric. Second, the phase margin is intrinsically insensitive. For relative drifts $\Delta R_r/R_r \in [-20\%, +40\%]$ and $\Delta L_m/L_m \in [-20\%, 0]$, with Γ kept at its nominal value, the numerically evaluated PM stays within $[77^\circ, 84.5^\circ]$ under ideal cancellation of the mechanical pole and within $[74^\circ, 82^\circ]$ with the capped integral time. This insensitivity is structural: because the plant zero always lies at twice the flux-pole frequency, the net phase lag of this pole–zero pair cannot exceed 19.5° whatever the value of τ_r, so the PM cannot fall below 70° under ideal cancellation. Finally, the viscous friction B (notoriously difficult

to identify in practice) affects neither property: it enters only through the integral cap $\tau_i = \min(J/B, \tau_i^{\max})$, which saturates at $\tau_i^{\max}$ for any realistic B, and through the plant pole at $-B/J$, three decades below ω_c. The design is, therefore, insensitive to B by construction.

4.6. Control Architecture

Figure 1 shows the complete architecture. The gain-scheduled PI produces a unified current reference i_s^*, from which the MTPA law (5) generates the dq references $i_{sd}^* = i_s^*$ and $i_{sq}^* = i_s^* \operatorname{sign}(T_e^*)$ tracked by conventional inner regulators. The gain-scheduling block computes K_p online from the flux-based scheduling variable $u_{0,\text{sched}}$ via (17), adding one division per sampling period over a fixed-gain MIMO-MTPA controller, with no look-up table or additional flux observer.

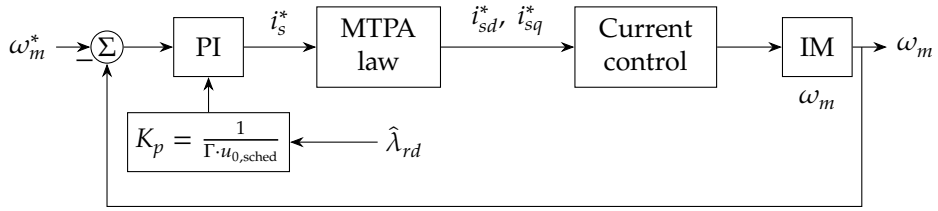

Figure 1. Proposed SISO-MTPA speed-control architecture.

5. Competing Strategies and Bandwidth Analysis

The SISO plant (13) and the gain-scheduled PI of Section 4 constitute the proposed controller. To evaluate its contribution, three alternative strategies are now introduced, each representing a different trade-off between efficiency and dynamic performance. All four controllers share identical inner-loop current regulators; only the outer-loop speed regulator and flux reference generation differ.

5.1. Classical FOC

In standard RFOC, the flux is maintained at its rated value $\lambda_{rd}^{\text{nom}}$. The speed plant reduces to the well-known first-order model $G_{\text{FOC}}(s) = K\lambda_{rd}^{\text{nom}}/(Js + B)$, which is LTI. A fixed-gain PI with pole-zero cancellation ($\tau_i = \min(J/B,\ \tau_i^{\max})$) yields an integrator-only open loop with PM $= 90^\circ$ and constant ω_c regardless of the load. Under partial load, however, the full magnetizing current still flows, causing high stator copper losses.

5.2. Fixed-Gain MIMO-MTPA

A natural first attempt at MTPA control is to enforce (5) as a reference law ($i_{sd}^* = |i_{sq}^*|$) while retaining a conventional fixed-gain PI speed controller. The resulting torque reference T_e^* then maps to the current references as follows:

$$i_s^* = \sqrt{|T_e^*|/K_T}, \qquad i_{sd}^* = i_s^*, \qquad i_{sq}^* = i_s^* \cdot \operatorname{sign}(T_e^*) \tag{21}$$

The PI gains are designed at the nominal MTPA operating point using the SISO plant (13). Note that the square root in (21) introduces a static nonlinearity in the reference path; its effect on large-signal performance is captured by the time-domain simulation in Section 6. Since these gains remain fixed, the effective loop gain $K_p \cdot KL_m u_0/J$ scales linearly with i_s. Consequently, the crossover frequency ω_c increases at high load and decreases at low load, degrading either the stability margins or the disturbance rejection depending on the load.

5.3. Loss-Minimization Benchmark

To provide a comprehensive efficiency benchmark, a loss-minimization (Loss-Min) strategy is also considered. While MTPA minimizes only the stator copper losses, Loss-Min minimizes the total electromagnetic losses [3,5,6,20]:

$$P_{\text{loss}} = \underbrace{\tfrac{3}{2}R_s|\boldsymbol{i}_s|^2}_{P_{\text{Cu},s}} + \underbrace{\tfrac{3}{2}R_r|\boldsymbol{i}_r|^2}_{P_{\text{Cu},r}} + \underbrace{P_{\text{Fe}}(\lambda_{rd}, \omega_m)}_{P_{\text{iron}}} \tag{22}$$

where the iron losses follow the simplified Steinmetz model $P_{\text{Fe}} = c_{\text{Fe}}\,\omega_e^2\,\lambda_{rd}^2$ [20]. The coefficient $c_{\text{Fe}} = 0.003\ \text{W s}^2/\text{Wb}^2$ was obtained from independent no-load characterization of the same machine, by fitting the measured iron losses and mapping the resulting model to this expression at 50 Hz (see Supplementary Material S1 for further details on the characterization procedure). For each torque-speed pair, the optimal d-axis current $i_{sd}^*(T_e, \omega_m)$ minimizing (22) is computed offline and stored in a two-dimensional look-up table (LUT).

The LUT spans $|T_e| \in [0, 150]$ N m and $\omega_m \in [-160, 160]$ rad/s on a 60×60 grid, corresponding to resolutions of approximately 2.54 N m and 5.42 rad/s, respectively. At each grid point, i_{sd} is swept from 2 to 30 A using 300 candidate values, and only solutions satisfying the stator-current constraint $|\boldsymbol{i}_s| \le 53$ A are retained; the resulting optimum is finally bounded below by $i_s^{\min} \approx 7$ A. During operation, the LUT is evaluated by linear interpolation, with torque and speed inputs saturated to the tabulated range.

Loss-Min retains the classical two-loop FOC architecture, applying i_{sd}^* (and the corresponding flux $\lambda_{rd}^* = L_m i_{sd}^*$) instead of the constant rated value, with its speed PI tuned on the nominal-flux FOC plant as is common practice [3,6]. The effective loop gain $K_p \cdot K\lambda_{rd}^*/J$, therefore, varies with the operating point: like MIMO-MTPA, Loss-Min exhibits a load-dependent crossover frequency, here because λ_{rd}^* departs from $\lambda_{rd}^{\text{nom}}$ rather than from the MTPA bilinear coupling. An analogous gain-scheduling correction would require feeding the LUT-defined flux estimate back into the speed loop; under MTPA, by contrast, the very constraint that yields the efficiency renders the gain dependence linear in the single operating-point variable u_0, the structural simplification exploited here.

5.4. Crossover Frequency Analysis: The Key Comparison

Table 3 summarizes the four control strategies. The critical distinguishing property is the behavior of ω_c as a function of the operating point. The four strategies occupy three cells of a two-by-two design space spanned by flux policy (rated vs. optimized) and bandwidth behavior (load-invariant vs. load-dependent ω_c): FOC achieves invariance by renouncing flux optimization, while MIMO-MTPA and Loss-Min achieve efficiency by renouncing invariance. The remaining cell (optimized flux *with* invariant bandwidth) is occupied only by the proposed SISO-MTPA.

Figure 2 presents the Bode plots of the speed-loop transfer function $L(s) = C(s) \cdot G(s)$ for all four strategies. The top subplot (magnitude) and middle subplot (phase) show the conventional frequency response at $u_0 = 5$ A (a representative low-load reel-out condition), while the bottom subplot (the key result of this analysis) sweeps the crossover frequency ω_c as a function of u_0 over the range 2–30 A:

FOC and SISO-MTPA both yield flat lines at $\omega_c = 20$ rad/s: FOC because the flux is constant (PM $\approx 87°$), and SISO-MTPA because the scheduling exactly cancels the gain dependence (PM $\approx 80°$, the deficit due to the pole-zero pair at $1/\tau_r$ and $2/\tau_r$ and the capped integral time). The fixed-gain strategies instead exhibit load-dependent bandwidth: MIMO-MTPA scales linearly with i_s, over-gained at high load ($\omega_c \approx 26$ rad/s at 30 A) and under-gained at low load ($\omega_c = 5.5$ rad/s at 5 A), while Loss-Min decreases nonlinearly as λ_{rd}^* departs from $\lambda_{rd}^{\text{nom}}$.

Table 3. Control Strategies Compared in This Work.

	FOC	MIMO-MTPA	SISO-MTPA	Loss-Min
Control architecture	Two-loop FOC	Single speed loop with feed-forward map	Single speed loop	Two-loop FOC with LUT
Flux-reference policy	Rated flux	MTPA relation	MTPA relation	Loss-optimal map
Optimization objective	None	Minimum stator copper loss	Minimum stator copper loss	Minimum total electromagnetic loss
Linearized speed plant	First-order LTI	Second-order LPV	Second-order LPV	First-order with variable gain
Gain scheduling	No	No	Yes	No
Crossover behavior	Constant	Proportional to i_s	Constant	Proportional to λ_{rd}^*
Required tuning/data	K_p, τ_i	K_p, τ_i, feed-forward map	Γ, τ_i	LUT, K_p, τ_i
Expected efficiency [a]	Baseline	High	High	Highest
Tracking performance [a]	Good	Degraded at partial load	Best (lowest RMSE)	Degraded at partial load

[a] Qualitative summary of the simulated and experimental results reported in Tables 4 and 5.

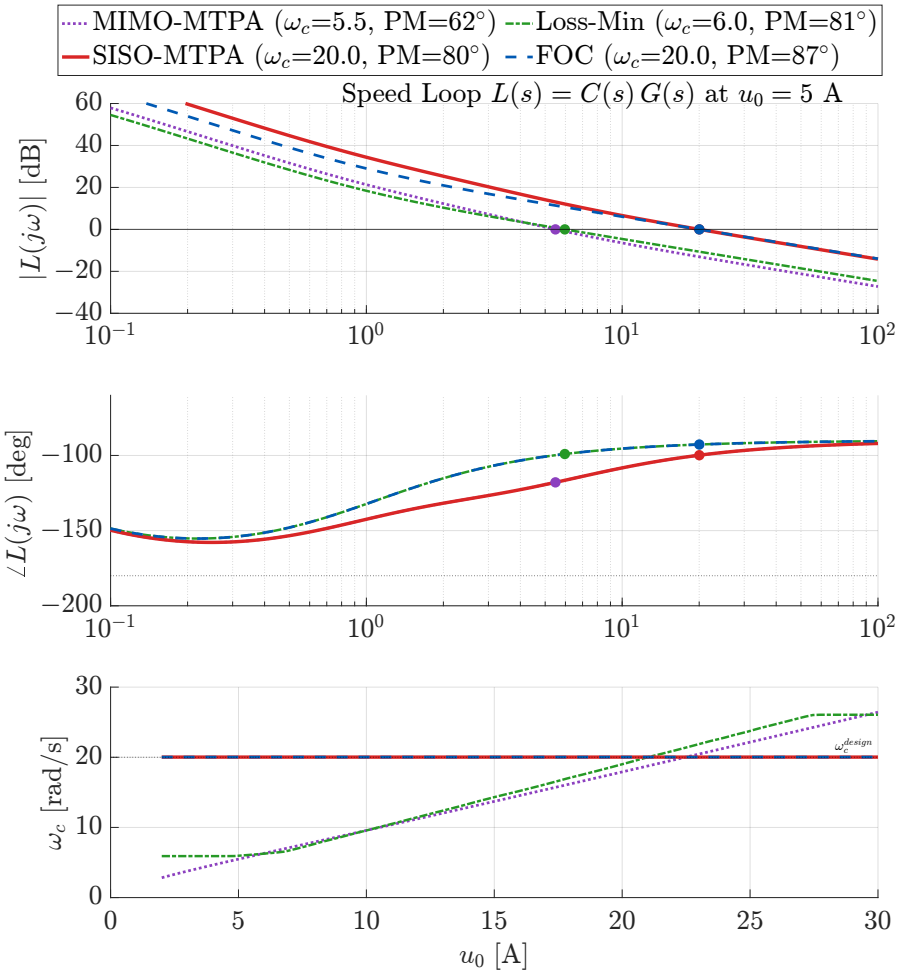

Figure 2. Speed-loop frequency response and crossover-frequency sweep. Top/middle: $L(s) = C(s)G(s)$ at $u_0 = 5$ A; bottom: ω_c versus u_0.

The bottom subplot provides a compact visual proof that only FOC and SISO-MTPA maintain constant bandwidth: FOC by keeping the flux constant (sacrificing efficiency), and SISO-MTPA by gain scheduling (achieving both MTPA efficiency and bandwidth invariance). In other words, the structural conflict between flux reduction and bandwidth identified in Section 1 is resolved (exactly within the adopted small-signal model, and with a single analytically derived constant) only by the proposed scheduling law.

6. Simulation of the AWES Pumping Cycle

6.1. Ground Station and Simulation Setup

The simulation is parameterized from the physical AWES ground station: a winch drum coupled to a Siemens 1LG4 186-4AA squirrel-cage IM (18.5 kW), fed by a two-level IGBT inverter at 10 kHz and controlled by a dSPACE MicroLabBox II at $T_s = 100\,\mu s$ with a 16384-pulse incremental encoder. The motor data in Table 1 correspond to this setup, also used for the experimental validation (Section 7).

During the pumping cycle, the drive alternates between generation (reel-out, IM in the second quadrant) and motoring (reel-in) [28]; as noted in Section 2, torque oscillations occur entirely on the electrical side, placing stringent demands on the dynamic response during phase transitions.

The simulation model includes the full nonlinear IM dynamics in the rotor-flux-oriented reference frame, ideal current control inner loops (an approximation justified in Section 2), a rotor flux observer based on the current model, and a first-order mechanical load model. Discretization is performed with a fixed simulation time step of 1 ms. All four controllers share identical inner-loop and flux observer implementations.

6.2. Pumping Cycle Profile

A simplified but representative pumping cycle is designed based on the operating principles documented for ground-generation AWES [25]:

- *Reel-out* (0–40 s): $\omega_m^* = +50$ rad/s, $T_L = 35$ N m.
- *Wind gust* (15–23 s): A symmetric triangular perturbation raises T_L from 35 to 55 N m and back over 8 s (peak-to-mean 1.6:1, consistent with measured tether profiles [34]); the peak remains below the MTPA saturation torque $K_T i_{sd,\mathrm{nom}}^2 = 58.7$ N m, with $i_{sd,\mathrm{nom}}$ the rated d-axis current (Table 1), keeping (13) valid.
- *Transition* (40–42 s): Speed reversal ($+50 \rightarrow -100$ rad/s) simultaneous with a load drop ($T_L : 35 \rightarrow 8$ N m), the most demanding condition for the speed controller.
- *Reel-in* (42–52 s): $\omega_m^* = -100$ rad/s, $T_L = 8$ N m.

The reel-out to reel-in duration ratio of 4:1 and the tether force ratio of approximately 4.4:1 are representative of operational AWES data [34]. The reel-in speed of 100 rad/s is about 65% of the rated mechanical speed ($\approx$153 rad/s for this four-pole machine), so the drive remains in the constant-torque region, below the field-weakening speed; the back-EMF, further reduced by the lower MTPA flux at the light reel-in load, stays within the inverter voltage limit.

6.3. Step-Response Validation

Before applying the cyclic load profile, a speed-reference step is evaluated at two equilibrium currents, $u_0 = 5$ A and $u_0 = 15$ A. This test isolates the operating-point dependence of the closed-loop dynamics. As Figure 3 shows, the normalized SISO-MTPA responses at the two currents are practically coincident. The result confirms in the time domain that the scheduled product $K_p u_0$ remains constant and, therefore, preserves crossover frequency and phase margin. Fixed-gain MTPA does not have this property: changing the operating current changes its loop gain and transient speed.

The AWES application is nevertheless dominated by load-torque disturbances rather than repeated speed-reference steps. The step test verifies bandwidth invariance cleanly; the pumping-cycle tests that follow evaluate the practically more important rejection of tether-force disturbances.

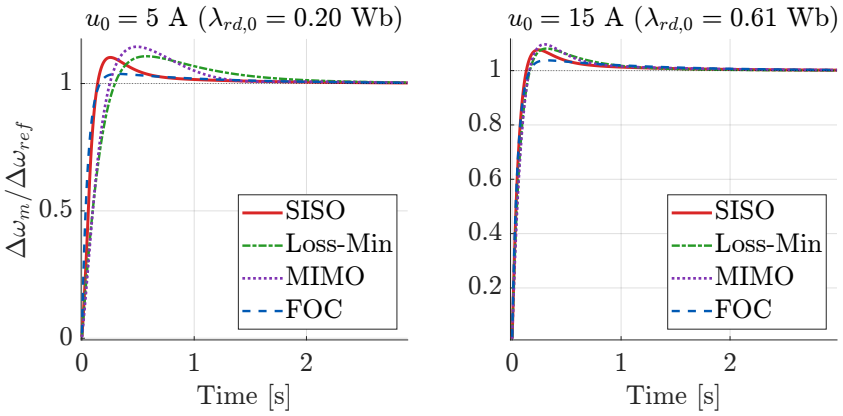

Figure 3. Simulated speed-reference step response at two representative MTPA operating currents, $u_0 = 5$ A and $u_0 = 15$ A. The nearly coincident SISO-MTPA responses demonstrate operating-point-invariant closed-loop dynamics.

6.4. Pumping-Cycle Results

Eight complete pumping cycles were simulated under the profile of the previous subsection. Figure 4 shows two of them and provides the full-cycle context, including the gust during reel-out and the large speed reversal between reel-out and reel-in. The closer disturbance-rejection windows are then examined in Figure 5. The principal observations are:

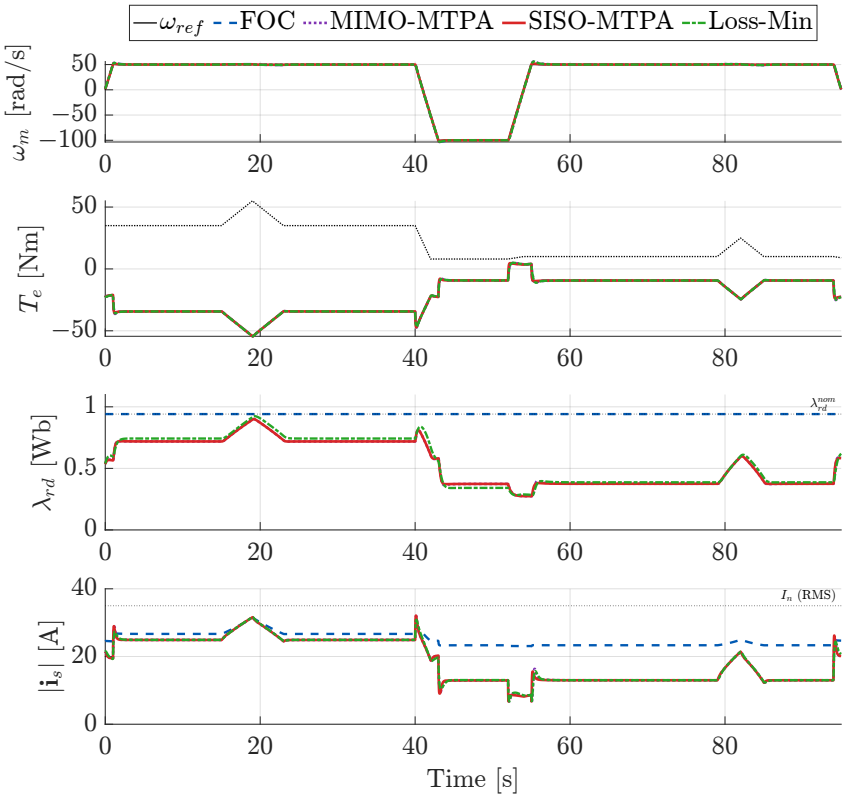

Figure 4. Simulation over two complete AWES pumping cycles. From top to bottom: rotor speed, electromagnetic and load torque, rotor flux, and stator-current magnitude. The triangular gust occurs during reel-out at 15–23 s; the transition beginning at $t = 40$ s combines a speed reversal with a load reduction.

1. *Speed tracking*: All four strategies track well during quasi-steady phases. The wind gust ($\Delta T_L = 20$ N m) and the reel-out to reel-in transition ($\Delta\omega_m = 150$ rad/s) differentiate the controllers. The SISO-MTPA exhibits the smallest speed excursions during both events, while MIMO-MTPA and Loss-Min show larger deviations, particularly during

low-wind gusts where their effective bandwidth drops below the design value (see detailed comparison in Figure 5).

2. *Rotor-flux behavior*: FOC holds $\lambda_{rd}^{\text{nom}} = 0.94\,\text{Wb}$ throughout. MIMO-MTPA and SISO-MTPA converge to the same MTPA flux $\lambda_{rd} = L_m i_s$ at a given load, but they follow different transient paths because only SISO-MTPA adapts the speed-controller gain. Loss-Min follows the independently optimized LUT flux trajectory.
3. *Stator-current demand*: The rated-flux FOC strategy continuously carries the rated magnetizing current $i_{sd,\text{nom}} = 23\,\text{A}$. During partial-load reel-out, the optimized strategies reduce the required current substantially; the MTPA cases operate at approximately 10–19 A over the range studied.

Figure 5 provides a detailed comparison of the load disturbance rejection at two representative operating points spanning the reel-out load range: high wind ($T_L = 35\,\text{N m}$, left) and a low-wind partial-load condition ($T_L = 10\,\text{N m}$, right). Two effects are visible. First, at both operating points the SISO-MTPA achieves smaller speed errors than FOC, despite both strategies having the same crossover frequency ($\omega_c = 20\,\text{rad/s}$); this advantage is due to the plant zero at $-2/\tau_r$, which provides additional loop gain in the gust frequency band (Section 6.6). Second, the MIMO-MTPA and Loss-Min speed errors increase markedly from high wind to low wind, because their effective bandwidth drops with $|\mathbf{i}_s|$, whereas the SISO-MTPA maintains the same error magnitude at both operating points.

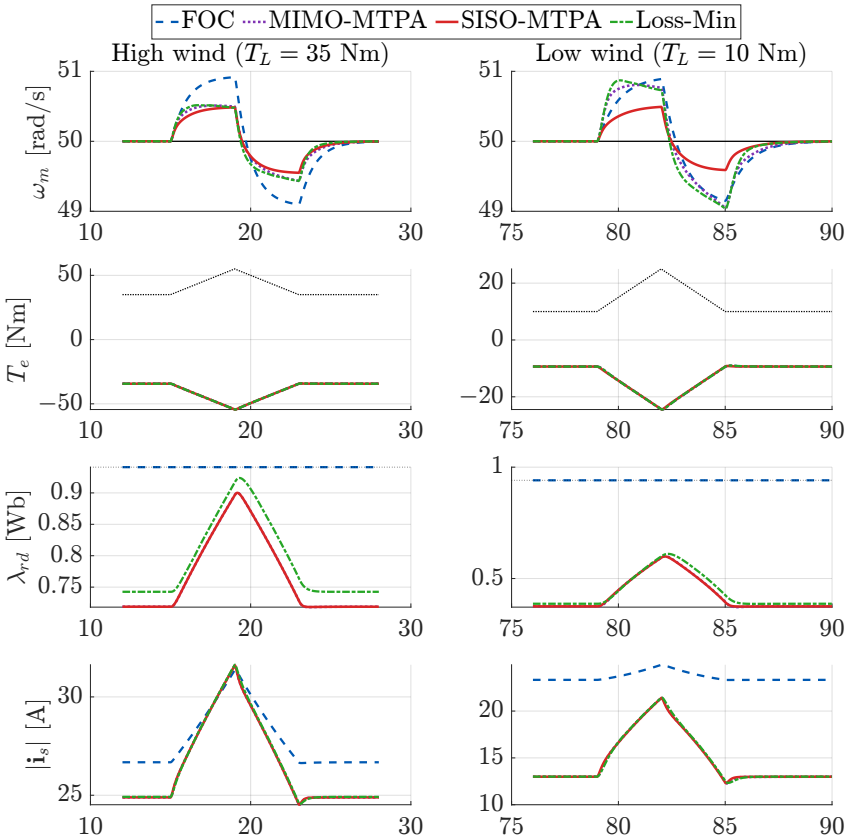

Figure 5. Load -disturbance rejection at high load, $T_L = 35\,\text{N m}$, and partial load, $T_L = 10\,\text{N m}$. Rows: speed, torque, rotor flux, and stator current.

6.5. Energy Balance and Efficiency

Table 4 reports the energy balance averaged over eight complete cycles. The cycle efficiency is defined as $\eta_{\text{cycle}} = E_{\text{net}}/E_{\text{out}}$, where E_{out} is the gross mechanical energy extracted during reel-out, E_{in} is the mechanical energy consumed during reel-in, and $E_{\text{net}} = E_{\text{out}} - E_{\text{in}} - E_{\text{loss}}$ is the net electrical energy harvested per cycle. This metric is inher-

ently low for pumping-cycle AWES because the reel-in phase consumes a substantial fraction of the reel-out energy [25]; the drive electromechanical efficiency $(1 - E_{\text{loss}}/(E_{\text{out}} + E_{\text{in}}))$ is 84% for the MTPA strategies versus 73% for FOC.

Table 4. Energy Balance Per Pumping Cycle (Average Over 8 Cycles).

	FOC	MIMO-MTPA	SISO-MTPA	Loss-Min
E_{out} (kJ)	47.17	47.15	47.13	47.14
E_{in} (kJ)	10.98	10.98	10.97	10.97
$E_{\text{Cu},s}$ (kJ)	11.06	6.58	6.58	6.61
$E_{\text{Cu},r}$ (kJ)	0.70	1.43	1.43	1.37
E_{Fe} (kJ)	3.77	1.10	1.10	1.11
E_{loss} (kJ)	15.53	9.11	9.11	9.09
E_{net} (kJ)	20.66	27.06	27.06	27.08
η_{cycle} (%)	43.8	57.4	57.4	57.4
$\max \lvert\Delta\omega_m\rvert$ (rad/s)	2.7	6.0	2.3	6.0

All three efficiency-oriented strategies reduce total losses by approximately 41% relative to FOC. The rotor copper losses *increase* under MTPA (from 0.7 to 1.43 kJ) due to higher slip, a known trade-off [13], but this is offset by the stator copper and iron loss reductions.

The dynamic metrics highlight the key result: SISO-MTPA achieves the smallest maximum speed deviation, with $\max \lvert\Delta\omega_m\rvert = 2.3$ rad/s—a >60% reduction versus MIMO-MTPA and Loss-Min, and even lower than FOC (2.7 rad/s).

6.6. Discussion

6.6.1. Origin of the Dynamic Advantage

The SISO-MTPA dynamic advantage has two sources. First, the implicit gain scheduling $K_p = 1/(\Gamma u_0)$ keeps the loop gain $KL_m/(\Gamma J)$ (and hence $\omega_c = 20$ rad/s and PM $\approx 80°$) constant at all operating points (Figure 2). Second, the plant zero at $-2/\tau_r = -4.88$ rad/s, absent in the zero-free FOC plant, boosts the loop gain and phase in the 2–5 rad/s band where the tether-force disturbance has significant content (the 8 s gust places odd harmonics at 2.4–5.5 rad/s). This frequency-domain alignment explains why SISO-MTPA achieves slightly smaller peak excursions than FOC (Table 4) despite a slightly lower phase margin.

6.6.2. Why Fixed-Gain Strategies Degrade at Partial Load

For the fixed-gain strategies, by contrast, the effective bandwidth collapses at partial load ($\omega_c \approx 9$ rad/s at $i_s \approx 10$ A for MIMO-MTPA, and similarly for Loss-Min as $\lambda_{rd}^{*} < \lambda_{rd}^{\text{nom}}$), as visible in Figure 5. This degradation is particularly consequential because partial load is not a benign corner of the AWES envelope: it corresponds precisely to low-wind reel-out and gust events, the very conditions in which disturbance rejection is most needed. Bandwidth invariance, therefore, means having the design bandwidth available *when it matters*, not only at rated load.

6.6.3. Efficiency–Dynamics Trade-Off and Validity Range

In terms of trade-offs (Table 3), the SISO-MTPA is thus the only strategy that improves *both* efficiency and dynamics relative to FOC (Section 5.4), with only two analytically derived tuning parameters. It operates within its domain of validity ($\lvert T_e\rvert \le K_T i_{sd,\text{nom}}^2 = 58.7$ N m) throughout the cycle; operation beyond this limit requires blending with classical FOC and is left for future work.

7. Experimental Validation

7.1. Laboratory Setup

The experimental validation is performed on the AWES ground-station bench (Figure 6) using the same 18.5 kW IM drive and control platform described in Section 6.



Figure 6. AWES ground-station test bench with the 18.5 kW IM, load machine, dSPACE MicroLabBox II, and IGBT inverter.

The phase-current signals are sampled at $T_s = 100\,\mu s$ and analog low-pass filtered before the dSPACE inputs by a fourth-order filter with a cutoff frequency of approximately 32 kHz ($\approx 2.0 \times 10^5$ rad/s). The control hardware, measurement chain, analog filters, and controller parameters of the experimental setup are detailed in Supplementary Material S1.

All four control strategies share identical inner current loops (bandwidth ≈ 1500 rad/s) and rotor flux observer implementations. The gain-scheduling law for SISO-MTPA uses the flux-based scheduling variable $u_{0,\mathrm{sched}}$ with the floor $i_s^{\min} \approx 7$ A defined in Section 4.

For consistency, all four strategies use the same nominal speed-loop design settings, $\omega_c = 20$ rad/s and $\tau_i = 1$ s. The electrical power used for the energy calculations is obtained from time-aligned voltage and current channels, compensating the relative delay of 0.28 ms between the voltage and current analog filters (Supplementary Material S1); this correction is particularly relevant for the FOC case because of its larger reactive-power component.

7.2. Realistic Pumping Cycle Profile

To complement the idealized simulation study of Section 6, the experimental validation employs a realistic torque profile derived from a high-fidelity aerodynamic simulation of a pumping kite system for a delta kite ($A = 1.83\,\mathrm{m}^2$, $m = 2\,\mathrm{kg}$) operating at a wind speed of 13 m/s using a literature-established AWES simulator [35]. The load machine reproduces the pre-recorded tether torque $T_L(t)$ while the speed reference $\omega_m^*(t)$ follows the corresponding reel-out/reel-in schedule. All four strategies are tested under the identical pre-recorded profile to ensure comparable operating conditions.

7.3. Experimental Results

Figure 7 presents the measured rotor speed, commanded load torque, stator current magnitude, and instantaneous electrical power of the induction machine for the four strategies during the reel-out and reel-in phases of a representative pumping cycle. The transition between these phases is omitted from the figure to improve clarity. The qualitative trends are consistent with the simulation results of Section 6, with quantitative differences attributable to parameter uncertainty, magnetic saturation, and inverter nonlinearities. To improve visualization, the electrical power traces are low-pass filtered using a moving-average filter with a 0.08 s window. This moving-average filtering is used only for visualization; all energy quantities reported in Table 5 are obtained by integrating the corresponding unfiltered sampled signals.

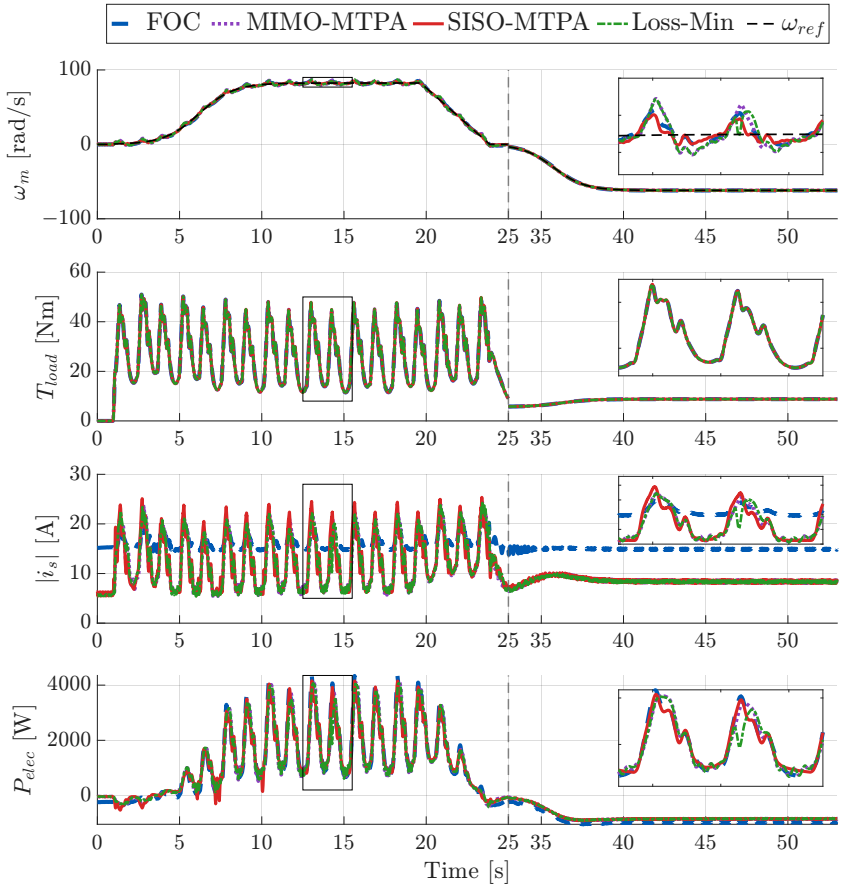

Figure 7. Experimental results under a realistic AWES pumping cycle (reel-out and reel-in phases). From top to bottom: rotor speed and reference, commanded load torque, stator current magnitude, and filtered electrical power.

Table 5 summarizes the experimental metrics for one AWES pumping cycle. Since only stator copper losses can be directly quantified from the available measurements, the comparison focuses on the accumulated copper energy $E_{Cu,s}$. The three optimization strategies significantly reduce copper losses with respect to the baseline FOC: MIMO-MTPA, SISO-MTPA, and Loss-Min achieve reductions of 57.1%, 55.6%, and 57.1%, respectively. These values are slightly higher than the $\approx$ 41% reduction predicted in simulation, which is attributed to the more realistic AWES-derived experimental profile and to non-ideal effects not captured in the simplified simulation model.

Table 5. Experimental Energy and Tracking Metrics for One AWES Pumping Cycle.

	FOC	MIMO-MTPA	SISO-MTPA	Loss-Min
$E_{\mathrm{Cu},s}$ (kJ)	13.01	5.58	5.77	5.58
E_{net} (kJ) *	6.36	13.70	12.92	13.65
max $\lvert\Delta\omega_m\rvert$ (rad/s)	3.846	5.044	2.938	4.986
Mean reel-out peak $\lvert\Delta\omega_m\rvert$ (rad/s)	2.93 $\pm$ 0.49	4.24 $\pm$ 0.62	2.30 $\pm$ 0.35	4.03 $\pm$ 0.69
Speed tracking RMSE (rad/s)	0.872	1.207	0.706	1.176

* Expanded uncertainty $\pm$5.5%, applicable to the net energy of the entire cycle; residual offsets after manual zeroing of the sensors are not included.

Despite achieving similar copper loss reductions and slightly lower net energy than Loss-Min in the experimental cycle, the proposed SISO-MTPA strategy provides significantly

improved dynamic performance. The maximum speed deviation during load transients, caused by the cyclic tether force variations inherent to pumping AWES operation, is reduced by 42% and 41% compared with MIMO-MTPA and Loss-Min, respectively. This behavior is consistent with the bandwidth invariance imposed by the proposed gain-scheduling law. Moreover, SISO-MTPA achieves a 19.1% lower speed tracking RMSE than the baseline FOC controller. Although each experimental record comprises a single pumping cycle, the reel-out phase contains 15–18 tether-force oscillations, providing repeated disturbance events within the same test. The event-wise statistics reported in Table 5 show that SISO-MTPA achieves both the lowest mean reel-out peak speed deviation and the lowest dispersion among the four strategies.

Two additional observations from Table 5 are worth discussing. First, the stator copper energy of SISO-MTPA (5.77 kJ) is 3.4% higher than that of MIMO-MTPA (5.58 kJ), although both enforce the same steady-state MTPA condition; this difference is attributed to the larger transient currents commanded by the gain-scheduled controller at partial load, and is the energetic counterpart of its superior disturbance rejection. Second, consistent with the simulation results, both MTPA strategies achieve net energy values comparable to the Loss-Min benchmark. The differences in net energy among the three efficiency-oriented strategies in Table 5 (below 0.8 kJ) are of the same order as the expanded uncertainty of the measurement, ±5.5% of the net energy of the entire cycle.

Overall, the experimental results confirm the intended role of SISO-MTPA. In the trade-off space of net harvested energy versus speed-tracking error (Table 5, Figure 8), no competing strategy dominates the proposed controller in both metrics simultaneously. At the same time, SISO-MTPA itself strictly dominates the FOC baseline, delivering twice its net energy with a lower speed-tracking RMSE. Despite achieving comparable net energy performance to MIMO-MTPA and Loss-Min, SISO-MTPA provides significantly improved speed tracking, with an RMSE approximately 1.7 times lower.

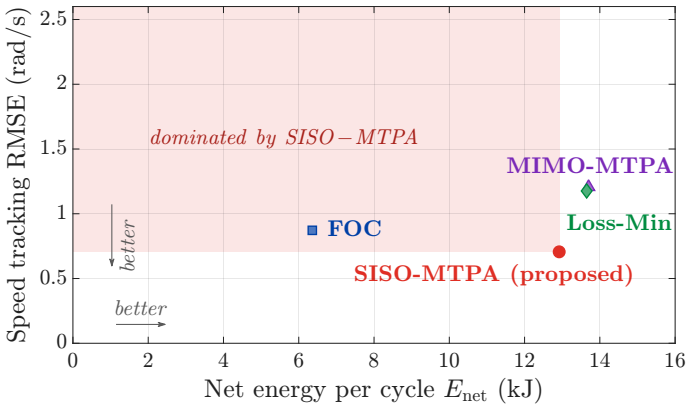

Figure 8. Experimental energy–tracking trade-off for the four strategies. The shaded region is dominated by the proposed SISO-MTPA.

7.4. Industrial Drive Benchmark During High-Power Reel-Out

To further assess the practical relevance of the proposed controller, an additional experiment was carried out against an ABB ACS880-01-061A-3 industrial drive based on direct torque control (DTC). The drive operated in its standard sensorless speed-control configuration, without encoder feedback, and received the speed reference through CAN communication with a 10 ms update period, the maximum rate of the implemented setup and of the drive-side logging. This interface is representative of an AWES ground station commanded by a supervisory kite controller over a fieldbus. The 10 ms update does not limit the ABB disturbance rejection, since its internal speed and current loops run at their native rates and the dominant tether-force dynamics are much slower than the supervisory

command-update rate. The ABB drive was tuned for efficient operation using its auto-identified motor data and flux-optimizing energy-saving mode. The complete parameter settings of the drive are listed in Supplementary Material S2.

Both controllers followed the same speed reference and torque profile imposed by the coupled load machine. The rotor speed used for evaluation was measured with the same encoder, although only the proposed controller used it for feedback.

The two drives, therefore, differ in their feedback path as well as in their control law: the ABB drive estimates speed internally, whereas SISO-MTPA closes the loop with the encoder speed measurement. Part of the RMSE difference may stem from this, so the comparison should be read as a system-level benchmark against a representative sensorless industrial configuration rather than as an isolated comparison of control laws. The comparison focuses on the high-power reel-out interval of the AWES cycle, 8–18 s in Figure 7, where most of the energy is produced and load-torque oscillations are most demanding. During the reel-in phase, the torque demand is low and nearly constant, and both drives track tightly.

Figure 9 shows the measured rotor speed and electrical power for SISO-MTPA and the ABB drive during the selected interval, and Table 6 summarizes the metrics. SISO-MTPA reduces the speed-tracking RMSE by 47% and the maximum speed deviation by 37%, while producing comparable generated energy.

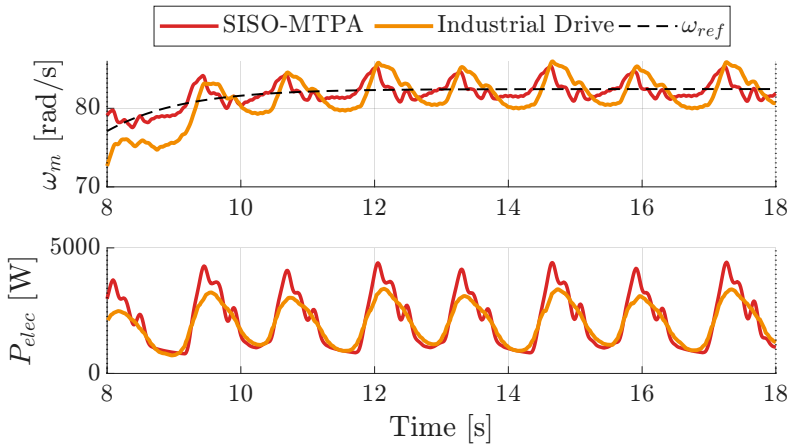

Figure 9. Experimental comparison with the ABB ACS880 during high-power reel-out. Top: rotor speed; bottom: electrical power.

Table 6. Experimental Comparison with the ABB Industrial Drive during High-Power Reel-Out.

Metric	SISO-MTPA	ABB ACS880
Speed tracking RMSE (rad/s)	1.15	2.17
max $\|\Delta\omega_m\|$ (rad/s)	3.15	4.99
Generated energy (kJ)	21.52	20.18

Thus, the relevant outcome is not an efficiency gain over the industrial drive, but comparable energy performance with markedly improved tracking under experimentally reproduced AWES conditions.

8. Conclusions

This paper has shown that the structural conflict between efficiency-oriented flux reduction and speed-loop bandwidth in induction motor drives admits an exact resolution under the MTPA constraint, within the adopted small-signal model and its operating region. Enforcing $i_{sd} = |i_{sq}|$ reformulates the conventional two-input FOC plant as a SISO system with a second-order transfer function and a real zero at $-2/\tau_r$, arising from the simultaneous

excitation of the flux and torque channels. The gain-scheduled PI law $K_p = 1/(\Gamma u_{0,\text{sched}})$ exploits this structure by canceling the operating-point dependence of the plant gain, maintaining $\omega_c = 20\,\text{rad/s}$ and PM $\approx 80^\circ$ from a single analytic scheduling constant.

A four-strategy comparison on an 18.5 kW IM drive in AWES pumping cycles (through both simulation with an idealized profile and experimental validation with a realistic AWES-cycle-based torque profile) has demonstrated that:

1. Only FOC and SISO-MTPA maintain constant bandwidth (FOC by sacrificing efficiency, SISO-MTPA by gain scheduling), confirmed both analytically and experimentally.
2. The distinguishing advantage of SISO-MTPA is its dynamic performance under efficiency-oriented operation: it achieves the lowest maximum speed deviation both in simulation (2.3 vs. 6.0 rad/s for MIMO-MTPA and Loss-Min) and experimentally (reductions of 42% and 41%, respectively), together with the lowest tracking RMSE among the optimized strategies. In the experimental energy–tracking plane, it is the only strategy that strictly dominates the FOC baseline while remaining undominated by any other.
3. In simulation, the three efficiency-oriented strategies reduce total electromagnetic losses by about 41% relative to FOC, raising efficiency from 73% to 84% and the net energy from 20.66 to 27.08 kJ. Experimentally, stator copper losses fall by 55–57% and the net energy rises from 6.36 to 12.92–13.70 kJ; the three efficiency-oriented strategies achieve comparable energy performance.
4. The SISO-MTPA needs only two analytically derived parameters (Γ, τ_i), no additional speed-loop flux observer, and no look-up tables. Experiments confirm its effectiveness under magnetic saturation, inverter nonlinearities, measurement noise, and thermal drift of R_r.
5. A focused benchmark against a tuned ABB ACS880 industrial drive during high-power reel-out, under the same speed reference, torque profile, and encoder measurement, showed 47% lower speed-tracking RMSE and 37% lower maximum deviation with comparable generated energy (within instrumentation uncertainty).

Combining MTPA efficiency, superior dynamic response, and implementation simplicity, the SISO-MTPA controller is particularly attractive for applications dominated by partial-load operation with frequent load transients, such as AWES pumping cycles, precisely the regime where fixed-gain efficiency strategies lose the bandwidth they were designed with.

Future work will address experimental characterization of the scheduling law under deep magnetic saturation and field weakening (extending the analytical sensitivity bounds of Section 4.5), and integration with the kite guidance and control system for AWES applications.

Supplementary Materials: The following supporting information can be downloaded at: https://www.mdpi.com/article/10.3390/electronics15214891/s1, Supplementary Material S1: Custom Control Hardware Setup and Relevant Parameters; Supplementary Material S2: Industrial ABB ACS880 Drive Parameter Settings.

Author Contributions: Conceptualization, D.S.-M.; methodology, D.S.-M. and C.N.-M.; software, D.S.-M. and C.N.-M.; validation, all authors; formal analysis, D.S.-M.; investigation, all authors; resources, D.S.-M. and J.G.-G.; data curation, C.N.-M. and M.A.-R.; writing—original draft preparation, D.S.-M. and C.N.-M.; writing—review and editing, all authors; visualization, C.N.-M. and M.A.-R.; supervision, D.S.-M. and C.N.-M.; project administration, D.S.-M.; funding acquisition, D.S.-M. All authors have read and agreed to the published version of the manuscript.

Funding: This research was funded by MICIU/AEI/10.13039/501100011033, grant number PID2025-173796OB-I00.

Institutional Review Board Statement: Not applicable.

Informed Consent Statement: Not applicable.

Data Availability Statement: The original experimental data presented in this study are openly available in Zenodo at https://doi.org/10.5281/zenodo.21130146 (accessed on 14 October 2026).

Acknowledgments: During the preparation of this manuscript, the authors used ChatGPT (GPT-6, OpenAI) and Claude (Claude Opus 5.5, Anthropic) for English-language editing. The authors reviewed and edited the output and take full responsibility for the content of this publication.

Conflicts of Interest: The authors declare no conflicts of interest.

Abbreviations

The following abbreviations are used in this manuscript:

AWES	Airborne wind energy system
DTC	Direct torque control
FOC	Field-oriented control
IM	Induction motor
LUT	Look-up table
MIMO	Multiple-input multiple-output
MTPA	Maximum torque per ampere
PI	Proportional–integral
RFOC	Rotor-flux-oriented control
RMSE	Root-mean-square error
SISO	Single-input single-output

Nomenclature

Symbol	**Meaning**	**Unit**
i_{sd}	d-axis stator-current component (flux producing)	A
i_{sq}	q-axis stator-current component (torque producing)	A
i_s	Unified nonnegative MTPA current, $i_s = i_{sd} = \lvert i_{sq}\rvert$	A
$\boldsymbol{i}_s$, $\lvert\boldsymbol{i}_s\rvert$	Stator-current vector and its Euclidean magnitude	A
$\boldsymbol{i}_r$, $\lvert\boldsymbol{i}_r\rvert$	Rotor-current vector and its Euclidean magnitude	A
λ_{rd}	Rotor d-axis flux linkage	Wb
ω_m, ω_m^*	Mechanical angular speed and its reference	rad/s
ω_e	Electrical angular frequency	rad/s
T_e, T_L	Electromagnetic torque and tether/load torque applied at the shaft	N m
L_m, L_{rr}	Magnetizing inductance and total rotor inductance	H
R_s, R_r	Stator and rotor resistances	Ω
J	Total inertia referred to the motor shaft	kg m^2
B	Viscous-friction coefficient	N m s/rad
$\tau_r = L_{rr}/R_r$	Rotor time constant	s
$\tau_m = J/B$	Mechanical time constant	s
p	Number of pole pairs	–
$k = L_m/L_{rr}$	Rotor–stator coupling factor	–
K	Electromagnetic torque coefficient in $T_e = K\lambda_{rd} i_{sq}$	N m/(Wb A)
$K_T = KL_m$	Steady-state torque coefficient under MTPA	N m/A^2
c_{Fe}	Coefficient of the simplified iron-loss model	W s^2/Wb^2
$P_{\mathrm{Cu},s}$, $P_{\mathrm{Cu},r}$	Stator and rotor copper losses	W
P_{Fe}, P_{loss}	Iron loss and total electromagnetic loss	W
K_p, τ_i	PI proportional gain and integral time constant	A s/rad; s
$\tau_i^{\max}$	Upper limit imposed on the integral time constant	s
ω_c	Speed-loop gain-crossover angular frequency	rad/s
Γ	Analytical constant used in $K_p = 1/(\Gamma u_0)$	rad/(A^2 s)
PM	Phase margin	degree
u_0	Equilibrium value of the unified MTPA current used for linearization	A
$u_{0,\mathrm{sched}}$	Practical gain-scheduling estimate of u_0, obtained from the estimated rotor flux	A
$i_s^{\min}$, $T_e^{\min}$	Minimum current floor and associated torque reserve	A; N m
$\Delta(\cdot)$	Small-signal perturbation about an equilibrium point	–

References

1. Leonhard, W. *Control of Electrical Drives*, 3rd ed.; Springer: Berlin/Heidelberg, Germany, 2001. [CrossRef]
2. Vas, P. *Sensorless Vector and Direct Torque Control*; Oxford University Press: Oxford, UK, 1998. [CrossRef]
3. Bazzi, A.M.; Krein, P.T. Review of methods for real-time loss minimization in induction machines. *IEEE Trans. Ind. Appl.* **2010**, *46*, 2319–2328. [CrossRef]
4. Kioskeridis, I.; Margaris, N. Loss minimization in induction motor adjustable-speed drives. *IEEE Trans. Ind. Electron.* **1996**, *43*, 226–231. [CrossRef]
5. Kirschen, D.S.; Novotny, D.W.; Lipo, T.A. Optimal efficiency control of an induction motor drive. *IEEE Trans. Energy Convers.* **1987**, *EC-2*, 70–76. [CrossRef]
6. Nicolás-Martín, C.; Montilla-DJesus, M.E.; Santos-Martín, D.; Martínez-Crespo, J. Computationally efficient and loss-minimizing model predictive control for induction motors in electric vehicle applications. *Energies* **2025**, *18*, 1444. [CrossRef]
7. Resa, J.; Cortes, D.; Marquez-Rubio, J.F.; Navarro, D. Reduction of induction motor energy consumption via variable velocity and flux references. *Electronics* **2019**, *8*, 740. [CrossRef]
8. Kousalya, V.; Singh, B. Optimized reference points based vector control of induction motor drive for electric vehicle. *IEEE Trans. Ind. Appl.* **2023**, *59*, 4164–4174. [CrossRef]
9. Goswami, G.; Das, S. An online efficient loss model controller for rotor-field oriented induction motor drives. *IEEE Trans. Energy Convers.* **2024**, *39*, 578–588. [CrossRef]
10. Goswami, G.; Das, S. Inherently robust loss model controller for energy efficient operation of indirect rotor field oriented induction motor drives. *IEEE Trans. Power Electron.* **2024**, *39*, 14951–14960. [CrossRef]
11. Mohebbi, M.R.; Arab Khaburi, D. Robust flux angle control of induction motors to improve efficiency at light loads. *IET Electr. Power Appl.* **2024**, *18*, 779–789. [CrossRef]
12. Balogun, A.; Olajube, A.; Awelewa, A.; Okafor, F.; Sanni, T.; Samuel, I. A sensorless efficiency-optimizing vector control scheme for an induction motor drive. *Front. Energy Res.* **2024**, *12*, 1406565. [CrossRef]
13. Wasynczuk, O.; Sudhoff, S.D.; Corzine, K.A.; Tichenor, J.L.; Krause, P.C.; Hansen, I.G.; Taylor, L.M. A maximum torque per ampere control strategy for induction motor drives. *IEEE Trans. Energy Convers.* **1998**, *13*, 163–169. [CrossRef]
14. Fereidooni, A.; Davari, S.A.; Garcia, C.; Rodriguez, J. Simplified predictive stator current phase angle control of induction motor with a reference manipulation technique. *IEEE Access* **2021**, *9*, 54173–54183. [CrossRef]
15. Peresada, S.; Kovbasa, S.; Dymko, S.; Bozhko, S. Dynamic output feedback linearizing control of saturated induction motors with torque per ampere ratio maximization. In Proceedings of the 2nd International Conference on Intelligent Energy and Power Systems (IEPS 2016), Kyiv, Ukraine, 7–11 June 2016; pp. 1–6. [CrossRef]
16. Bozhko, S.; Dymko, S.; Kovbasa, S.; Peresada, S.M. Maximum torque-per-amp control for traction IM drives: Theory and experimental results. *IEEE Trans. Ind. Appl.* **2017**, *53*, 181–193. [CrossRef]
17. Mosaddegh Hesar, H.; Abootorabi Zarchi, H.; Ayaz Khoshhava, M. Online maximum torque per ampere control for induction motor drives considering iron loss using input–output feedback linearisation. *IET Electr. Power Appl.* **2019**, *13*, 2113–2120. [CrossRef]
18. Kuczmann, M.; Horváth, K. Tensor product alternatives for nonlinear field-oriented control of induction machines. *Electronics* **2024**, *13*, 1405. [CrossRef]
19. Popov, A.; Popova, V.; Gulyaev, I.; Briz, F. Dynamic response of FOC induction motors using MTPA considering voltage constraints. In Proceedings of the 26th International Workshop on Electric Drives: Improvement in Efficiency of Electric Drives (IWED 2019), Moscow, Russia, 30 January–2 February 2019; pp. 1–5. [CrossRef]
20. Attaianese, C.; Di Monaco, M.; Tomasso, G. Maximum torque per watt (MTPW) field-oriented control of induction motor. *Electr. Eng.* **2021**, *103*, 2611–2623. [CrossRef]
21. Hasan, F.A.; Rashad, L.J. Combining fractional-order PI controller with field-oriented control based on maximum torque per ampere technique considering iron loss of induction motor. *AIMS Electron. Electr. Eng.* **2024**, *8*, 380–403. [CrossRef]
22. Chowdhury, R.R.; Koperundevi, G.; Venkadesan, A. Simplified MTPA integrated virtual voltage vector-based MPCC for improved performance and efficiency in IM drive-based electric vehicles. *IEEE Trans. Transp. Electrif.* **2025**, *11*, 6753–6762. [CrossRef]
23. Peresada, S.; Tilli, A.; Tonielli, A. New passivity-based speed-flux tracking controllers for induction motor. In Proceedings of the 26th Annual Conference of the IEEE Industrial Electronics Society (IECON 2000), Nagoya, Japan, 22–28 October 2000; pp. 1099–1104. [CrossRef]
24. Schmehl, R. (Ed.) *Airborne Wind Energy: Advances in Technology Development and Research*; Springer: Singapore, 2018. [CrossRef]
25. Loyd, M.L. Crosswind kite power. *J. Energy* **1980**, *4*, 106–111. [CrossRef] [PubMed]
26. Sommerfeld, M.; Dörenkämper, M.; De Schutter, J.; Crawford, C. Impact of wind profiles on ground-generation airborne wind energy system performance. *Wind Energy Sci.* **2023**, *8*, 1153–1178. [CrossRef]
27. Joshi, R.; Schmehl, R.; Kruijff, M. Power curve modelling and scaling of fixed-wing ground-generation airborne wind energy systems. *Wind Energy Sci.* **2024**, *9*, 2195–2215. [CrossRef]

28. Fagiano, L.; Milanese, M.; Piga, D. Optimization of airborne wind energy generators. *Int. J. Robust Nonlinear Control* **2012**, *22*, 2055–2083. [CrossRef]
29. Rapp, S.; Schmehl, R.; Oland, E.; Haas, T. Cascaded pumping cycle control for rigid wing airborne wind energy systems. *J. Guid. Control Dyn.* **2019**, *42*, 2456–2473. [CrossRef]
30. van der Vlugt, R.; Peschel, J.; Schmehl, R. Design and experimental characterization of a pumping kite power system. In *Airborne Wind Energy*; Ahrens, U., Diehl, M., Schmehl, R., Eds.; Springer: Berlin/Heidelberg, Germany, 2013; pp. 403–425. [CrossRef]
31. Uppal, A.A.; Fernandes, M.C.R.M.; Vinha, S.; Fontes, F.A.C.C. Cascade control of the ground station module of an airborne wind energy system. *Energies* **2021**, *14*, 8337. [CrossRef]
32. Weber, J.; Marquis, M.; Cooperman, A.; Draxl, C.; Hammond, R.; Jonkman, J.; Lemke, A.; Lopez, A.; Mudafort, R.; Optis, M.; et al. *Airborne Wind Energy*; Technical Report NREL/TP-5000-79992; National Renewable Energy Laboratory (NREL): Golden, CO, USA, 2021. [CrossRef]
33. Nicolás-Martín, C.; Santos-Martín, D.; DeLosRíos-Navarrete, F.; González-García, J. Airborne wind energy system test bench electrical emulator. *Wind Energy Sci.* **2025**, *10*, 2279–2297. [CrossRef]
34. Fechner, U.; van der Vlugt, R.; Schreuder, E.; Schmehl, R. Dynamic model of a pumping kite power system. *Renew. Energy* **2015**, *83*, 705–716. [CrossRef]
35. Sánchez-Arriaga, G.; García-Villalba, M.; Schmehl, R. Modeling and dynamics of a two-line kite. *Appl. Math. Model.* **2017**, *47*, 473–486. [CrossRef]

Disclaimer/Publisher's Note: The statements, opinions and data contained in all publications are solely those of the individual author(s) and contributor(s) and not of MDPI and/or the editor(s). MDPI and/or the editor(s) disclaim responsibility for any injury to people or property resulting from any ideas, methods, instructions or products referred to in the content.